Binuclear Lanthanide Complexes Based on 4-Picoline- N -oxide: From Sensitized Luminescence to Single-Molecule Magnet Characteristics

Senthil Kumar Kuppusamy, Eufemio Moreno-Pineda, Aline Nonat, Benoît Heinrich, Lydia Karmazin, Loïc Charbonnière, Mario Ruben

Binuclear lanthanide complexes based on 4-Picoline-N-oxide: from sensitised luminescence to single-molecule magnet characteristics

Senthil Kumar Kuppusamy,[a]* Eufemio Moreno-Pineda,[b]* Aline M. Nonat,[c]* Benoît Heinrich,[d] Lydia Karmazin,[e] Loïc J. Charbonnière,[c] and Mario Ruben[a,f,g]*

a. *Institute of Quantum Materials and Technologies (IQMT), Karlsruhe Institute of Technology (KIT), Hermann-von-Helmholtz-Platz 1, 76344 Eggenstein-Leopoldshafen, Germany.*
b. *Depto. de Química-Física, Facultad de Ciencias Naturales, Exactas y Tecnología, Universidad de Panamá, 0824, Panamá.*
c. *Equipe de Synthèse pour l'Analyse, IPHC, UMR 7178, CNRS-Université de Strasbourg, ECPM, 25 rue Becquerel, 67087 Strasbourg Cedex, France.*
d. *Institut de Physique et Chimie des Matériaux de Strasbourg (IPCMS), CNRS-Université de Strasbourg, 23, rue du Loess, BP 43, 67034 Strasbourg cedex 2, France.*
e. *Service de Radiocristallographie, Fédération de Chimie Le Bel FR2010 CNRS-Université de Strasbourg, 1 rue Blaise Pascal, BP 296/R8, 67008 Strasbourg cedex, France.*
f. *Institute of Nanotechnology (INT), Karlsruhe Institute of Technology (KIT), Hermann-von-Helmholtz-Plats 1, D-76344 Eggenstein-Leopoldshafen, Germany.*
g. *Centre Européen de Sciences Quantiques (CESQ), Institut de Science et d'Ingénierie, Supramoléculaires (ISIS), 8 allée Gaspard Monge, BP 70028, 67083 Strasbourg Cedex, France.*

*Correspondence to: senthil.kuppusamy2@kit.edu; eufemio.moreno@up.ac.pa; aline.nonat@unistra.fr; mario.ruben@kit.edu

ABSTRACT

Lanthanide complexes featuring luminescent and/or single-molecule magnet (SMM) characteristic(s) are proposed candidates to develop molecule-based spintronics, memory, and quantum information processing (QIP) device architectures. Herein, we report on the luminescent and/or SMM characteristic(s) of charge-neutral binuclear lanthanide complexes—$[Ln_2Cl_6(4\text{-picNO})_4(\mu_2\text{-}4\text{-picNO})_2]\cdot 2H_2O$ (Ln^{3+} = Tb^{3+} ([Tb_2]) or Dy^{3+} ([Dy_2]); 4-picNo

= 4-picoline N-oxide). The Dy and Tb complexes show 4-picNO-sensitised luminescence with quantum yields of 0.14% and 88%, respectively, in the solid-state. The luminescent Dy complex is an SMM with magnetisation reversal barrier (U_{eff}) = 20.6(4) cm^{-1} under zero applied magnetic field, whereas the Tb complex is not an SMM. Dipolar interaction mediated weak anti-ferromagnetic coupling between the Ln^{3+} centres operates at low temperatures. The facile preparation of $[Ln_2Cl_6(4\text{-picNO})_4(\mu_2\text{-}4\text{-picNO})_2]\cdot 2H_2O$ complexes showing high luminescence quantum yield (Tb^{3+}) and SMM characteristic (Dy^{3+}) might prove useful toward the designing of analogues luminescent-SMM hybrids suitable for technological applications.

INTRODUCTION

Lanthanide (Ln^{3+}) complexes exhibiting Single-molecule magnet (SMM)[1–3] and/or line-like emission behaviour[4,5] are plausible molecular systems for the fabrication of miniaturised information storage[1,6–8], computing[9–12], and spintronics[13–17] device architectures *via* bottom-up self-assembly approaches. Consequently, continuous efforts to modulate the SMM[18–23] and luminescent properties[24,25] of Ln^{3+} complexes by ligand field tuning and molecular energy level engineering, respectively, are in progress to harness the applications potential of the Ln^{3+} complexes[26,27].

Lanthanide-SMMs (Ln-SMMs) featuring characteristic large intrinsic magnetic anisotropy and slow relaxation of the magnetisation are two-level systems that could perform as a quantum bit (qubit)—the quantum unit of information[10,12,28–30]. While the classical binary digits (bits) are limited to values of 0 or 1, qubits can additionally take-up superposition of 0 or 1, that is, the state of a single qubit is a linear combination of 0 and 1, offering enhanced information processing ability compared to classical bits. Coupling of individual qubits in arrays is a strategy adopted to fabricate quantum gates for quantum computing applications[31–33]. However, difficulties inherent to the inter-qubit coupling limits the utility of such strategy. As an alternative, for example, the exponential extension of Hilbert space[31] can be achieved employing the nuclear states of the lanthanides by designing bi- or multi-nuclear isotopologues Ln-SMMs[9,10,31]. The hyperfine coupling between the nuclear spin and the ground doublet in Ln-SMMs composed of isotopically enriched Ln^{3+} centres, for example ^{163}Dy (I = 5/2) or the indirect coupling of nuclear states[10,34], produces different quantum states (extension of Hilbert space), enabling the construction of

multilevel systems termed as qu*d*its, where $d > 2$[34–36]. The hyperfine split qu*d*it levels are addressed taking advantage of the quantum tunnelling of magnetisation (QTM), as exemplified in the case of prototypical Tb-complexes[10,16,34,37]. It is evident that a binuclear SMM could function as a multilevel qu*d*it system in the presence of QTM and hyperfine interactions, and such a system is desirable for quantum information processing (QIP) applications[10,34].

In addition to the SMM property, Ln^{3+}-based, for example, Ln^{3+} = Eu, Tb, Dy, Er, or Yb, mono-, bi-, and multi-nuclear complexes feature intense, long-lived, and line-like sensitised emission bands covering the whole visible and IR spectral range[4,5,24,38–43]. The alluring emission characteristics render luminescent Ln^{3+} complexes suitable for developing multifunctional[26,27] molecule-based optical data-storage and communication systems[44–47]. Crucially, the emission properties coupled with the presence of nuclear spins enable the creation of Ln^{3+}-molecule-based coherent light-matter interfaces. Such interfaces can be leveraged to demonstrate the quantum information processing utility of the luminescent lanthanide complexes. Recently, we have reported on the creation of coherent light-matter interfaces in binuclear and mononuclear Eu^{3+} complexes[48,49]. We have shown that spectral holes can be burnt in the electric dipole-induced $^5D_0$-to-$^7F_0$ transition, enabling the estimation of optical coherence lifetime (T_2) and polarization of nuclear spins in one of the ground-state hyperfine levels[48]. Moreover, by taking advantage of the ultranarrow $^5D_0$-to-$^7F_0$ inhomogeneous linewidth associated with a mononuclear Eu^{3+} complex, we have demonstrated storage of photons inside a molecular crystal, rendering the complex as an optically addressable molecular memory. Crucially, the utility of the Eu^{3+} complex as a scalable qubit architecture—useful for performing quantum gate operations—has been elucidated by quantifying controlled ion-ion interactions between the Eu^{3+} centres[49]. All the prototypical demonstrations listed above elucidate the QIP utility of the Ln^{3+}-based molecular systems.

It is evident from the above discussions that Ln^{3+} complexes featuring SMM and/or luminescent characteristics are useful systems for developing application-oriented materials[50,51]. Ln^{3+} systems featuring both SMM and luminescent properties are ideal model systems to probe magneto-luminescence correlations, which may lead to light addressable SMMs both in the bulk and on the surface[52–55]. By analysing the fine structure associated with the luminescent line corresponding to the ground state term, for example, m_J = 15/2 in

Dy^{3+}, induced by ligand field (Stark splitting), the energy separation between the ground and excited m_J levels can be inferred as has been demonstrated[56,57]. On the other hand, the narrow spectral linewidths associated with Ln^{3+} systems could be leveraged to develop QIP systems.

In this context, we have extended on our previous report concerning $[Eu_2Cl_6(4\text{-picNO})_4(\mu_2\text{-}4\text{-picNO})_2]\cdot 2H_2O$ and prepared two new binuclear complexes—$[Ln_2Cl_6(4\text{-picNO})_4(\mu_2\text{-}4\text{-picNO})_2]\cdot 2H_2O$; Ln = Tb^{3+} [Tb_2] or Dy^{3+} [Dy_2] and studied their magnetic and luminescent characteristics, as detailed in the following sections.

RESULTS AND DISCUSSION

Synthesis and crystal structures

The binuclear Ln^{3+} complexes discussed in this study are prepared by following a procedure reported for $[Ln_2Cl_6(4\text{-picNO})_4(\mu_2\text{-}4\text{-picNO})_2]\cdot 2H_2O$ (Ln = Eu^{3+} or Gd^{3+})[48]. See experimental section for more details.

X-ray crystallographic analyses revealed that the complexes crystallise in the centrosymmetric $P\overline{1}$ space group belonging to triclinic crystal system (Table S1). As a representative example, the crystal structure of $[Dy_2Cl_6(4\text{-picNO})_4(\mu_2\text{-}4\text{-picNO})_2]\cdot 2H_2O$ is detailed (Figure 1), and the crystal structure and related parameters of $[Tb_2Cl_6(4\text{-picNO})_4(\mu_2\text{-}4\text{-picNO})_2]\cdot 2H_2O$ is depicted in the supporting information (Figure S1 and Table S1). The neutral [Dy_2] is composed of six 4-picNO and six chloride ligands. The O_4Cl_3 coordination environment around each Dy^{3+} ion is best described as pentagonal bipyramidal with a continuous shape measure (CShM) of 1.513. The equatorial positions (edges) of each pentagonal bipyramid are occupied by two monodentate 4-picNO ligands in *trans* fashion, one chloride ligand, and two μ_2-4-picNO ligands. The axial positions of each pentagonal bipyramid are occupied by the remaining chloride ligands. The Dy-O bond lengths range from 2.264(3) Å to 2.461(2) Å. The Dy-O bond lengths involving monodentate 4-picNO ligands are shorter than the Dy-O bond lengths associated with the μ_2-4-picNO ligands. The Dy-Cl bond lengths, with values ranging from 2.6598(10) Å to 2.7000(9) Å, are longer than the Dy-O bond lengths. The Dy-Cl bond lengths—2.6598(10) Å and 2.6714(10) Å—of the *axial* chloride ligands are shorter than the equatorial Dy-Cl bond length—2.7000(9) Å. The

intramolecular Dy-Dy and the shortest intermolecular Dy-Dy distances are 4.2237(4) Å and 8.3813(6) Å, respectively.

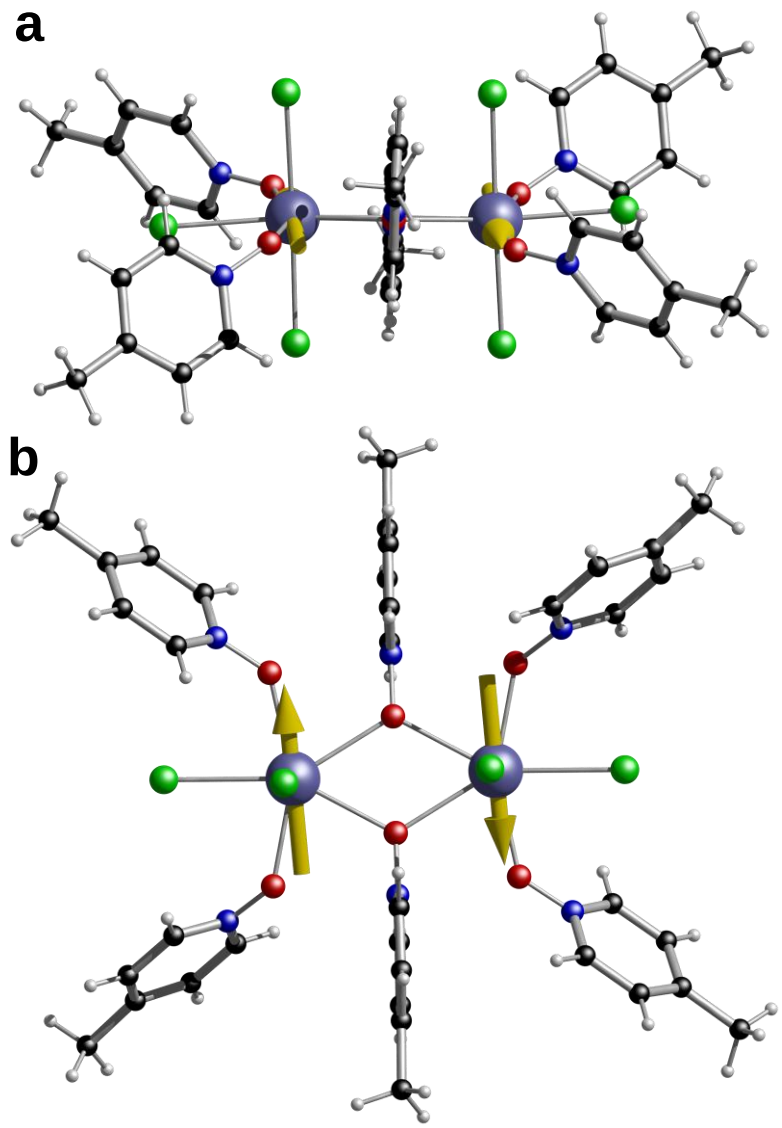

Figure 1. X-ray crystal structure of $[Dy_2Cl_6(4\text{-picNO})_4(\mu_2\text{-}4\text{-picNO})_2]\cdot 2H_2O$. a) side view and b) top view. The arrows show the direction of the principal axis of the *g*-tensor in the ground Kramer doublet of the Dy-complex, obtained from CASSCF calculations. Colour code: Dy, blue; C, black; Cl, green; O, red; H, light grey.

The Tb complex showed similar Ln-O, Ln-O(μ_2), and Ln-Cl bond lengths as observed for [Dy_2]. Intramolecular Tb-Tb and shortest intermolecular Tb-Tb distances of 4.2270(4) Å and 8.3727(5) Å, respectively, are observed.

In the crystal lattice, the complex molecules—[Dy_2] or [Tb_2]—arrange into layers in the b×c plane with two co-crystallized water molecules (Figure S2), according to oblique $P\bar{1}$

lattice (one molecule per asymmetric unit). Successive layers superpose with constant lateral shift leading to single-layer periodicity and triclinic structure with one molecule per unit cell.

Powder X-ray diffraction (PXRD) studies

To study the phase purity of the crystalline complexes, PXRD measurements of the complexes were performed. A good match observed between the PXRD and single-crystal (SCXRD) patterns (Figure 2) of the complexes elucidates the phase purity of the crystalline complexes. Comparable unit cell parameters (Table S2) obtained from the indexing of the PXRD and SCXRD data serve as an additional proof confirming the phase purity of the complexes.

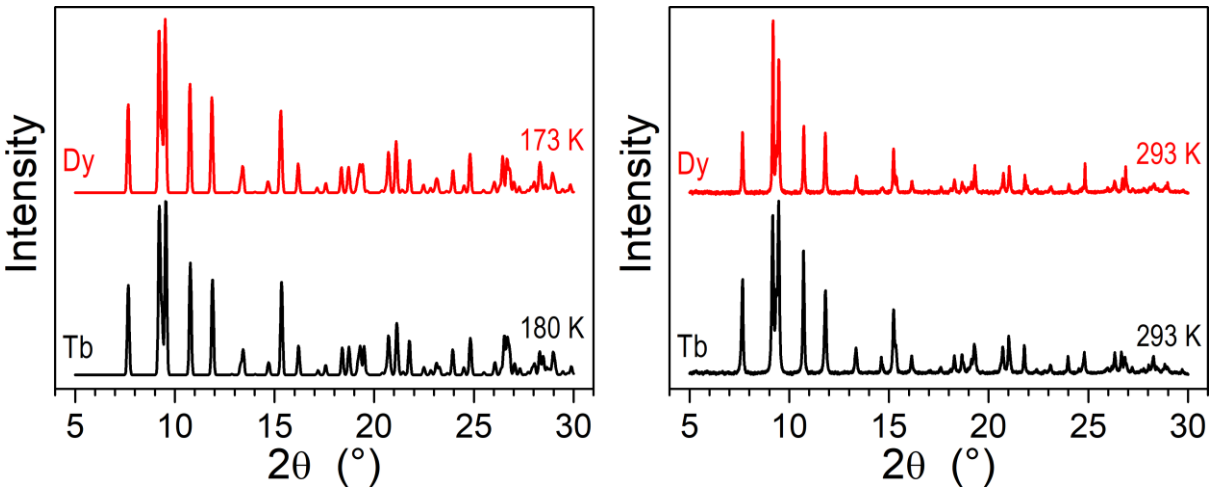

Figure 2. left: XRD patterns of [Dy_2] and [Tb_2] at 173 K and 180 K, respectively, calculated from the single-crystal X-ray structures of the complexes; right: experimental PXRD patterns at room temperature. All patterns are composed of the same reflections with only small changes in peak position and intensity, in relation with small variations of lattice parameters and electron densities.

In the powder, the molecular volume regularly decreases, at a mean rate of 4.3 $Å^3$ per atomic number, from Eu-to-Dy (Table S2), which involves decrease of layer spacing ($\Delta d/d$ jumps of 0.13-0.14%) and of lateral distances ($\Delta(\sqrt{A})/\sqrt{A}$) jumps of 0.11-0.12%). Single-crystal structures follow analogous trends (Table S2), although parameter values are more dispersed. The cell volume, sublattice area, and layer spacing vary with the nature of the Ln^{3+} ion, within respectively 1.5%, 1.2% and 0.5% in the powder structures. At the same

time, the √*A*/*d* ratio is nearly constant (1.179 ± 0.001), as well as parameter *a* of in-plane arrangement (66.61 ± 0.04°) and the shift of successive molecular layers related to b and c (3.20 ± 0.03 Å). This confirms the equivalence of all structures, with only small changes of lattice parameters.

Photophysical studies

The photoluminescence characteristics of the complexes were studied in the solid-state by exciting the 4-picNO-based transition centred at ~330 nm. At room temperature, [Tb_2] showed a bright luminescence corresponding to the $^5D_4 \rightarrow {}^7F_J$ (J = 6-3) transitions with weaker emission bands in the 640-660 nm region corresponding to J = 2 to 0 (Figure 3a). A high quantum yield of 88% (Table 1) evidences a very good sensitisation of the $^5D_4$ level of Tb^{3+} by 4-picNO. The PL of the terbium complex decays monoexponentially with a lifetime of 1.32 ms (Figure S3), indicating the presence of a single emissive species. The Dy complex showed weak Dy^{3+} centred emission bands at 485 nm ($^4F_{9/2} \rightarrow {}^6H_{15/2}$), 577 nm ($^4F_{9/2} \rightarrow {}^6H_{13/2}$), 663 nm ($^4F_{9/2} \rightarrow {}^6H_{11/2}$), 754 nm ($^4F_{9/2} \rightarrow {}^6H_{9/2}$) and 833 nm ($^4F_{9/2} \rightarrow {}^6H_{7/2}$) as shown in Figures 3a and S4a. A quantum yield of ~ 0.14% and lifetime (τ) <10 µs were observed upon ligand excitation at 339 nm at room temperature; accurate determination of the lifetime was prevented by low signal intensity. At 77K, a lifetime of 4.8 µs could be determined (Figure S4b). A low-symmetry crystal field around Dy^{3+} in [Dy_2] is inferred from the PL spectrum shown in Figure 2. The intensity of the blue $^4F_{9/2} \rightarrow {}^6H_{15/2}$ magnetic dipole transition centred at 485 nm hardly varies with crystal field around Dy^{3+} ions, whereas the electric dipolar transition ($^4F_{9/2} \rightarrow {}^6H_{13/2}$) at 577 nm is hypersensitive to Dy^{3+} coordination environment and is dominant for low local-site symmetry species, according to the Judd–Ofelt theory[58]. The observation of weak emission around 665 nm ($^4F_{9/2} \rightarrow {}^6H_{11/2}$) also evidences the low-symmetry of the crystal field around Dy^{3+} in [Dy_2].

a)

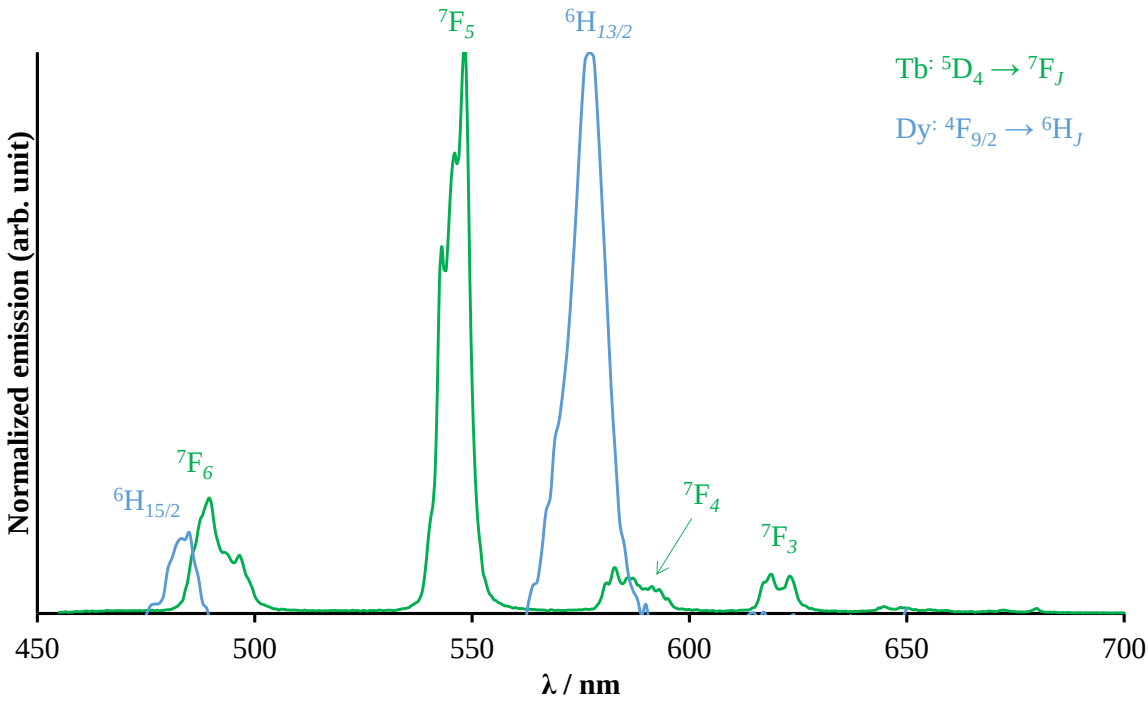

b)

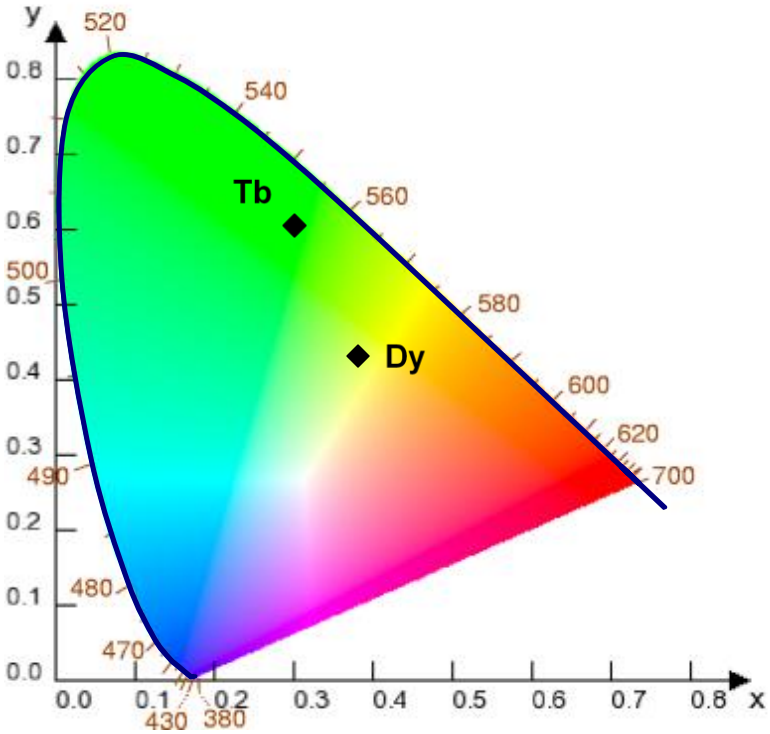

Figure 3. Steady-state emission characteristics of [Tb_2] and [Dy_2]. a) Normalised RT emission spectra of [Tb_2] (λ_{ex} = 330 nm) and [Dy_2] (λ_{ex} = 339 nm) complexes in the solid-state

and b) the Commission Internationale de l'éclairage (CIE) colour space chromaticity diagram of the complexes in the solid state (Tb: x = 0.3032, y = 0.6092; Dy: x = 0.3835, y = 0.4325).

Table 1. Selected photophysical data of [Tb_2] and [Dy_2] complexes in the solid-state.

Complex	ΔE (cm^{-1})	τ_{obs} (μs)[a]	$\phi_{tot\ (\%)}$[b]
Tb_2	3310	1330	88
Dy_2	2980	<10	0.14

[a]λ_{exc} = 330 nm for [Tb_2] and 339 nm for [Dy_2]. [b]Error for the absolute determination of quantum yield is estimated to be ± 15%.

The observed trends in the luminescence sensitization emission from the [Tb_2] and [Dy_2] can be rationalized considering the triplet energy (E_T) of 4-picNO antenna. An E_T = 23810 cm^{-1} (420 nm) was estimated, as reported in our previous study[48]. The triplet level of 4-picNO is located above the receiving levels of Tb^{3+} ($^5D_4$ = 20500 cm^{-1}) and Dy^{3+} ($^4F_{9/2}$ = 20830 cm^{-1}). This implies that the energy transfer from the triplet level of 4-picNO to the $^5D_4$ and $^4F_{9/2,}$ receiving levels of Tb^{3+} and Dy^{3+}, respectively, led to the sensitised luminescence. The total ligand to metal sensitisation energy transfer efficiency (η_{sens}) depends on the energy gap (ΔE) between the triplet state of the donor and Ln^{3+} acceptor states. An energy gap of 2500 cm^{-1} < $\Delta E(^3\pi\pi - {}^5D_4)$ < 4000 cm^{-1} is reported ideal for the luminescence sensitisation of Tb^{3+}. The high PL quantum yield of 88% observed for [Tb_2] is likely facilitated due to an optimal energy separation—ΔE ~ 3310 cm^{-1}—between the triplet level of 4-PicNO and $^5D_4$ acceptor level of Tb^{3+}. On the other hand, an optimal ΔE is not established for Dy^{3+} complexes. The presence of thermally accessible levels lying above the receiving $^4F_{9/2}$ level and the possible thermal back-energy transfer between the $^4F_{9/2}$ level and energetically close-lying excited levels is attributed as a contributing factor, decreasing the sensitised luminescence quantum yield of Dy-complexes[53].

Magnetic properties of the complexes

Direct current (DC) magnetic susceptibility studies of the previously reported [Gd_2][48], [Tb_2], and [Dy_2] complexes were carried out in an applied field (H_{dc}) = 0.1 T. At 300 K, $\chi_M T$ values of 15.8 ([Gd_2]), 28.1 ([Dy_2]), and 23.4 ([Tb_2]) cm^3 K mol^{-1} are observed (Figures 4 and S5). The $\chi_M T$ values are in the range expected for two uncoupled lanthanide ions. For [Gd_2],

the $\chi_M T$ versus T plot stays practically constant upon cooling down to ~10 K. Further cooling resulted in a decrease of the $\chi_M T$ product due to antiferromagnetic interactions (*vide infra*). A gradual decrease of $\chi_M T$ product is observed for the [Tb_2] and [Dy_2] complexes down to 100 K. Cooling the samples further causes a faster decrease of the $\chi_M T$ products, indicating the depopulation of the crystal field levels and/or antiferromagnetic interactions.

The field (H) dependence of molar magnetisation (M(H)) of the complexes were studied in the temperature and field-range of 2 to 5 K and 0 to 7 T, respectively. For [Gd_2], saturation of the magnetisation is reached at fields larger than 3 T. The M(H) = 13.9 N_b is practically identical to the Brillouin function for two uncoupled Gd^{3+} ions (Figure 4a, inset), indicating a negligible interaction between the ions. M(H) values of 9.2 and 9.8 N_b, at an applied magnetic field of 7 T (T = 2 K), were observed for the [Tb_2] and [Dy_2] (Figure 4b, inset) complexes, respectively.

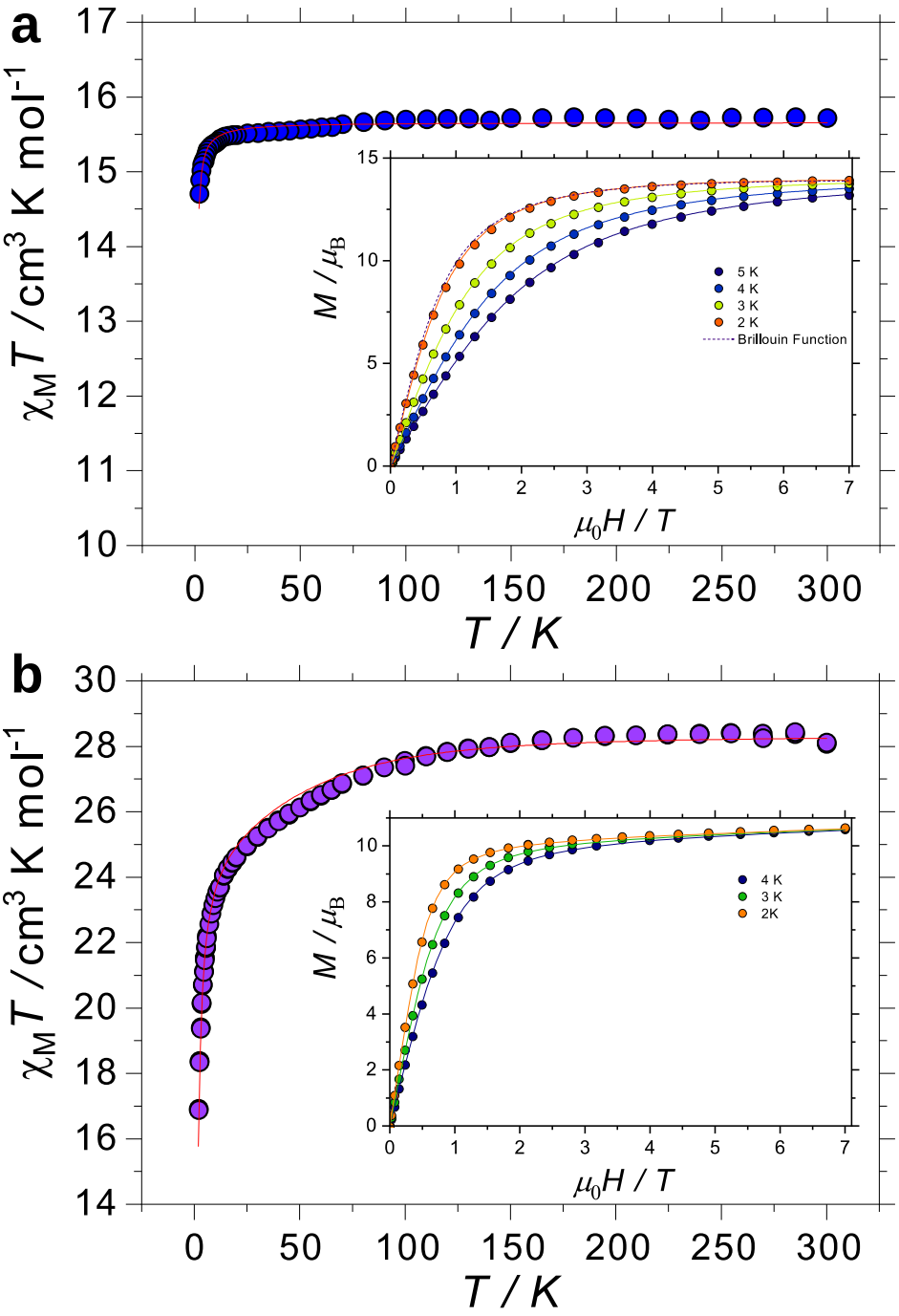

Figure 4. a) Experimental $\chi_M T(T)$ plot of [Gd_2] at an applied DC field of 0.1 T and magnetisation ($M(H)$) (inset) (solid symbols) and simulations (solid lines) obtained after simultaneous fitting employing equation 1; b) Experimental $\chi_M T(T)$ plots of [Dy_2] at H_{DC} = 0.1 T and magnetisation ($M(H)$) (inset) (solid symbols) and simulations (solid lines) obtained by simultaneous fitting employing equation 1, CF parameters obtained from CASSCF calculation, and an isotropic interaction connecting the spin part of the Dy(III) ions.

The downturn in the $\chi_M T$ profile for Gd_2 can be quantified by fitting magnetic susceptibility data and the $M(H)$ employing equation 1:

$$H = -2J\hat{S}_1\hat{S}_2 + g\mu_B H\sum_{i=1}^{2}\hat{S}_i \qquad \text{eq. (1)}$$

where the first term is the isotropic interaction connecting the spins and the second is the Zeeman term. Simultaneous fitting[59] yields an exchange coupling (*J)* value of –13 m K (–0.01 cm^{-1}) with *g* = 1.99 (Figure 4). The magnitude of *J* obtained from fitting procedure is in the range (J_{dip} = –0.01 cm^{-1}) expected for dipolar interactions associated with two Gd^{3+} centres. At this stage, no further analysis of the magnetic data for the systems based on anisotropic lanthanide ions is possible.

To assess the SMM behaviour of the complexes, alternating current (AC) magnetic susceptibility measurements were performed in an oscillating field of 5 Oe. No SMM characteristics were found for the Tb complex, as inferred from the absence of clear peaks in the out-of-phase (χ") susceptibility measurements (Figure S6). In contrast, a frequency and temperature dependence of the magnetic susceptibility, characteristic of SMM behaviour, were observed for [Dy_2] at zero applied magnetic field (Figure 5a). Application of an optimal DC magnetic field of 600 Oe (Figure S7 and Table S3) resulted in the shifting of the χ" peaks to a low frequency regime, as depicted in Figure 5b.

At zero applied magnetic field, temperature $\chi_M''(T)$ and frequency dependent $\chi_M''(\nu)$ out-of-phase magnetic susceptibilities, were observed for [Dy_2]. Temperature dependence of relaxation time ($\tau(T)$) was extracted by fitting the $\chi_M''(\nu)$ data to a modified Debye process between 2 K and 7 K. As shown in Figure 5b, a linear trend is observed above 5 K, which is characteristic of the Orbach process, whereas quantum tunnelling of magnetisation (QTM) is active below 4 K. The $\tau(T)$ can be fitted by equation 2:

$$\tau^{-1} = \tau_0^{-1}\exp\left[-U_{eff}/T\right] + CT^n + \tau_{QTM}^{-1} \quad \text{eq. (2)}$$

where, the first, second, and third terms represent the Orbach, Raman, and QTM processes, respectively. Fitting the data for the Dy complex at H_{DC} = 0 affords: U_{eff} = 29.7(1) K, τ_0 = 2.92(6)x10^{-6} s, *C* = 0.0042(6) s^{-1} K^{-n}, *n* = 6.236 and τ_{QTM} = 3.54(5)x10^{-4} s. Application of an optimal DC field of 600 Oe reduces the relaxation rate (Figure 5b and c). Fitting of the $\tau(T)$ plot obtained at H_{DC} = 600 Oe yields the following parameters: U_{eff} = 39.2(1) K, t_0 = 2.18x10^{-6} s, *C* = 0.0026(1) s^{-1} K^{-n}, *n* = 6.685(2) and χ_{QTM} = 0.032(2) s.

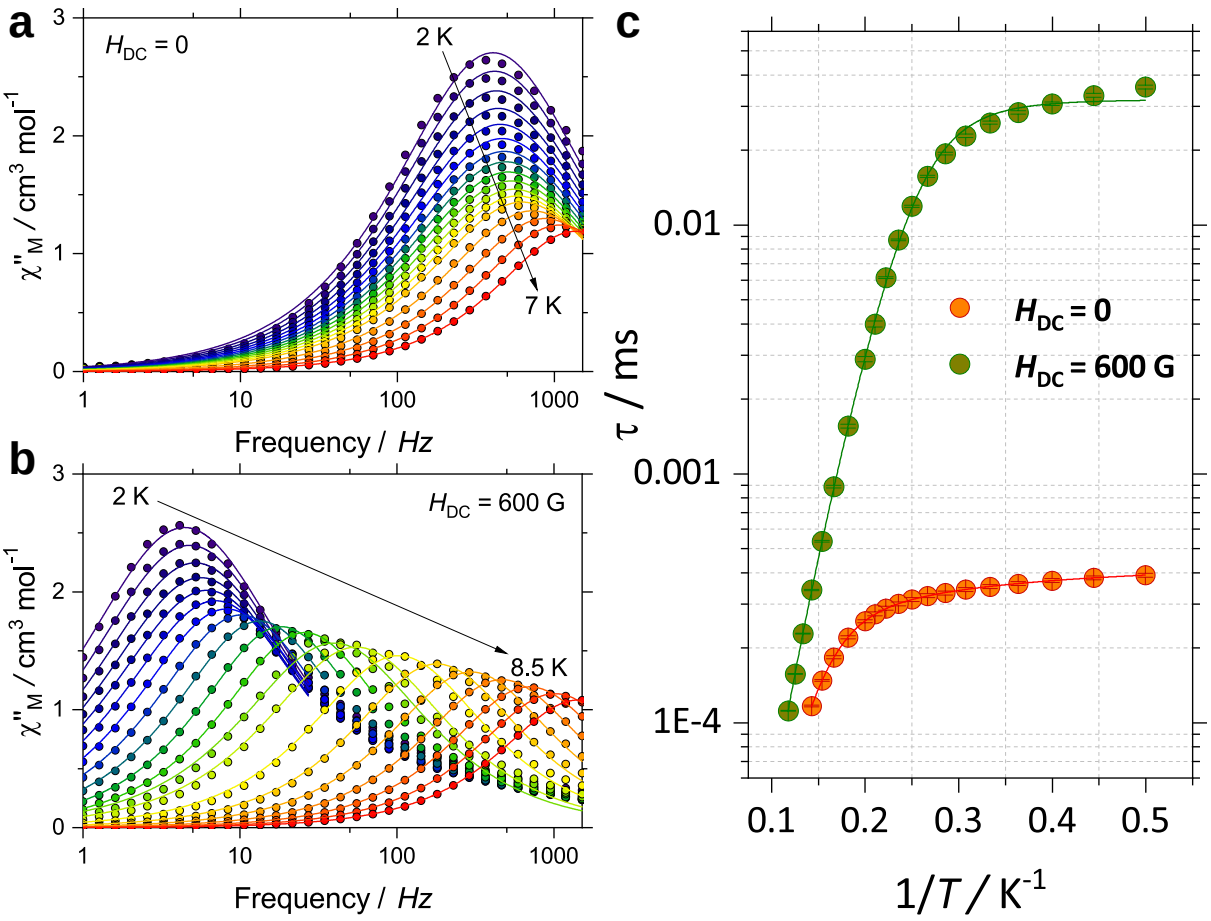

Figure 5. Single-molecule magnet characteristics of [Dy_2]. a) $\chi_M''(\nu)$ at zero applied magnetic field and; b) $\chi_M''(\nu)$ for H_{DC} = 600 Oe; c) temperature dependence of the relaxation times $\tau(T)$, (symbols) and the fitting using equation 2 and parameters in the text. The corresponding $\chi_M'(\nu)$ and Cole-Cole plots are shown in Figures S8 and S9.

To gain further insight into the magnetisation blocking of the Dy complex, *ab initio* calculations were performed with the CASSCF/SO-RASSI/SINGLE_ANISO approach implemented in the Molcas 8.2 program package[60–62]. For this purpose, the atomic coordinates of the Dy complex obtained from the single-crystal study were used without further optimisation. The energies of the low-lying Kramer's doublets and the main components of the *g* tensor of the Dy^{3+} is given in Table 2. The main magnetic axis (*z*) on the Dy ions is indicated in Fig. 1 by the yellow arrow, which is perpendicular to Cl. The g-values, g_x = 0.1. g_y = 0.3 and g_z = 19.43, indicate the axial nature of ground state doublet. The first excited state lies at 76 cm^{-1} and the second excited state is at 101 cm^{-1}, subsequent excited states are mixed and lie in the range of 155 to 330 cm^{-1} above the ground state doublet. The ground state doublet can be described as m_J = ±15/2, whilst the first excited state is mainly

±13/2 (97%). The average matrix elements of magnetic moment between the electronic states suggests the most efficient magnetic relaxation pathway to occur *via* the first excited state at 76 cm^{-1} (110 K). As observed, the U_{eff} = 20.64 cm^{-1} (H_{DC} = 0 Oe) obtained from dynamic studies is lower than the separation (ΔE = 76 cm^{-1}) of the ground and first excited state, indicating the importance of anharmonic processes in the relaxation of the complexes[63], while application of an optimal field reduces relaxation leading to ΔE ~ 40 cm^{-1}.

Table 2. *ab initio* energy barrier and principal g-tensor for the Kramer doublets of [Dy_2].

ab initio energy **(cm^{-1})**	***ab initio energy*** **(K)**	g_x	g_y	g_z	***Angle (°)***
0	0	0.1070	0.2223	19.4381	-
76.0	109.4	0.33685	1.1329	16.5012	121.6
101.2	145.6	0.9737	3.9503	11.3464	147.1
155.3	223.4	3.0891	6.2096	9.3338	98.7
200.9	289.1	0.3617	2.9396	10.9491	86.8
260.3	374.5	1.0746	2.4783	13.9358	101.4
286.7	412.5	1.1822	3.5791	13.7718	75.8
326.5	469.8	0.7302	0.0355	17.5599	55.7

The wavefunction for the ground state is 99% $|\pm 15/2\rangle$, while the first excited state is 97% $|\pm 13/2\rangle$ + 2% $|\pm 11/2\rangle$.

Employing the crystal field parameters obtained from the CASSCF calculation and connecting the two anisotropic Dy^{3+} ions via an isotropic exchange interaction, via the Lines model, we were able to simultaneously fit the $\chi_M''(T)$ and $M(H)$ data with an exchange Ising Hamiltonian of the form:

$$\widehat{H}_{ex} = J_{Lines}(\hat{s}_{1,z} + \hat{s}_{2,z}) \quad \text{eq. (3)}$$

where J_{Lines} is the exchange interaction connecting the spin part of the Dy^{3+}, that is, S = 5/2. We are able to reproduce the data sets with J_{Lines} = –0.04 cm^{-1} (Figure 4b). Comparison of the dipolar interaction between the Dy^{3+} and the J_{Lines} suggests that the interaction between the spins is purely of dipolar origin.

CONCLUSIONS

A new set of stable and charge-neutral binuclear lanthanide complexes of molecular formula $[Ln_2Cl_6(picNO)_4(\mu_2\text{-}picNO)_2]\cdot 2H_2O$ (Ln = Tb or Dy) was synthesised. Crystal structure analyses of the complexes revealed pentagonal bipyramidal geometry around the lanthanide ions. The 4-picNO ligand photosensitises the Tb^{3+} and Dy^{3+} centred emission; with total PL quantum yields of 88% ($[Tb_2]$) and 0.14% ($[Dy_2]$) were determined in the solid-state. The optimal energy gap (ΔE = ~3310 cm^{-1}) between the ligand-centred triplet (donor) and Tb^{3+}-centred $^5D_4$ receiving level facilitated efficient Tb-centred emission. From the SMM front, the Dy-complex functioned as SMM in the absence of applied magnetic field, and the application of a small DC field (600 Oe) slightly increased the spin-reversal barrier by suppressing the QTM. No out-of-phase susceptibility peaks were observed for the $[Tb_2]$ complex at zero and applied magnetic fields, indicating the absence of the slow relaxation of the magnetisation in the complex. Fitting of the *M*(*H*) plot of the Gd_2-complex with a Hamiltonian involving isotropic exchange interaction revealed the presence of weak intramolecular dipolar interaction mediated antiferromagnetic coupling between the constituent Gd^{3+}-centres. The magnitude of such antiferromagnetic coupling might account for the fast relaxation characteristics of the Dy-complex. Further, the weakly luminescent nature of the $[Dy_2]$ complex coupled with the not so well resolved fine structure of the $^4F_{9/2} \rightarrow {}^6H_{15/2}$ luminescence band centred at 485 nm rendered difficult the possibility to establish a magneto-optical correlation based on PL measurements. Overall, the easy-to-prepare nature of the complexes, the high 88% PL quantum yield obtained for the Tb-complex, and the SMM characteristic of the Dy-complex in the absence of applied magnetic field are the salient aspects of this study.

Experimental section

Materials

4-picoline N-oxide, $TbCl_3\cdot 6H_2O$, $DyCl_3\cdot 6H_2O$, and the solvents used in this study are received from commercial sources and used as received.

General procedure for the synthesis of the $[Ln_2Cl_6(PicNO)_4(\mu_2\text{-}PicNO)_2]\cdot 2H_2O$ (Ln = Tb and Dy) complexes

To a solution of 0.35 g (3.2 mmol) of 4-picoline N-Oxide in 12 mL of H_2O, 1.07 mmol of $LnCl_3.6H_2O$ (Ln = Tb or Dy) was added as a solid. The reaction mixture was stirred for 10 min and water was evaporated from the reaction mixture under reduced pressure. The solids were re-dissolved in 15 mL of hot EtOH, filtered, and the filtrate was cooled to RT. About 15-20 mL of EtOAc was carefully added to the filtrate until the formation of slight turbidity/precipitate, and the mixture was filtered to obtain a clear solution. The clear solution was left undisturbed for a few days in a closed vial. The procedure yielded X-ray quality crystals of $[Ln_2Cl_6(picNO)_4(\mu_2\text{-}picNO)_2]\cdot 2H_2O$ (Ln = Tb or Dy) in about 60% yield. The crystalline complexes are stable and can be stored and handled at ambient conditions.

Elemental analysis:

$[Tb_2Cl_6(picNO)_4(\mu_2\text{-}picNO)_2]\cdot 2H_2O$: Calculated for $C_{36}H_{42}Cl_6Tb_2N_6O_6\cdot 2H_2O$, C 35.4, H 3.8, N 6.88; Found C 34.93, H 3.73, N 6.76.

$[Dy_2Cl_6(picNO)_4(\mu_2\text{-}picNO)_2]\cdot 2H_2O$: Calculated for $C_{36}H_{42}Cl_6Dy_2N_6O_6\cdot 2H_2O$, C 35.20, H 3.77, N 6.84 ; Found C 35.07, H 3.70, N 6.78.

X-ray crystallography

X-ray diffraction data of $[Tb_2Cl_6(PicNO)_4(\mu_2\text{-}PicNO)_2]\cdot 2H_2O$ was collected employing a STOE StadiVari 25 diffractometer with a Pilatus300 K detector using GeniX 3D HF micro focus with MoKα radiation (λ = 0.71073 Å). The structure was solved using direct methods and was refined by full-matrix least-squares methods on all F_2 using SHELX-2014 implemented in Olex2. The crystals were mounted on a glass tip using crystallographic oil and placed in a cryostream. Data were collected using φ and ω scans chosen to give a complete asymmetric unit. All non-hydrogen atoms were refined anisotropically. Hydrogen atoms were calculated geometrically riding on their parent atoms.

For $[Dy_2Cl_6(PicNO)_4(\mu_2\text{-}PicNO)_2]\cdot 2H_2O$ complex, X-ray diffraction data collection was carried out on a Bruker APEX II DUO Kappa-CCD diffractometer equipped with an Oxford Cryosystem liquid N_2 device, using Mo-Kα radiation (λ = 0.71073 Å). The crystal-detector distance was 38 mm. The cell parameters were determined (APEX3 software; M86-EXX229V1 APEX3 User Manual", Bruker AXS Inc., Madison, USA, 2016) from reflections taken from three sets of 12 frames, each at 10 s exposure. The structure was solved using the program SHELXT-2014.[64] The refinement and all further calculations were carried out using SHELXL-2014.[65] Hydrogen atoms were included in calculated positions and treated as

riding atoms using SHELXL default parameters. The non-hydrogen atoms were refined anisotropically, using weighted full-matrix least-squares on F^2.

Magnetism

DC magnetic susceptibility measurements were performed using Quantum Design MPMS®3 and MPMS- XL SQUID magnetometers on crystalline material in the temperature range of 2 – 300 K under an applied DC magnetic field (*H*) of 1000 Oe. DC data were corrected for diamagnetic contributions from the eicosane and core diamagnetism employing Pascal's constants. Magnetisation as a function of applied field was investigated in the field and temperature ranges of 0 – 7 T and 2 – 10 K, respectively, at a sweep rate of 700 Oe/min. AC data was collected using an oscillating magnetic field of 5 Oe and frequencies between 1 and 1.5 kHz.

Photophysical studies

Steady state emission and excitation spectra were recorded on a FLP920 spectrometer from Edinburgh Instrument working with a continuous 450 W Xe lamp and a red sensitive Hamamatsu R928 photomultiplier in Peltier housing. All spectra were corrected for the instrumental functions. When necessary, high pass filters at 330 nm, 395 nm, 455 nm or 850 nm were used to eliminate the second order artefacts.

Phosphorescence lifetimes were measured on the same instrument working in the Multi Channels Spectroscopy (MCS) mode and using a Xenon flash lamp as the excitation source. Errors on lifetimes are ±10%. Luminescence quantum yields were measured with a G8 Integrating Sphere (GMP SA, Switzerland) according to the absolute method detailed in the literature[66]. Estimated errors are ±15%.

Low temperature measurements were performed with the help of an OptistatDN2 thermocryostat from Oxford Instruments controlled by a MercuryiTC temperature controller and with a turbopump form HiCUBE.

Computational details

The atoms were described using standard basis sets from the ANO-RCC library available in Molcas. For the lanthanide ion a basis set of VTZP quality employed, whilst VDZP quality was used for the atoms directly attached to the lanthanide ions, and VDZ quality for all

remaining atoms. The molecular orbitals (MOs) were optimized in state-averaged CASSCF calculations. For this, the active space for Dy complex was defined by the nine 4f electrons in the seven 4f orbitals of Dy^{3+}. Three calculations were performed independently for each possible spin-state, where 21 roots were included for *S* = 5/2, 224 roots were included for *S* = 3/2, and 490 roots were for *S* = 1/2 (RASSCF routine). The wavefunctions obtained from these CASSCF calculations were posteriorly mixed by spin-orbit coupling, where all 21 *S* = 5/2 states, 128 of the *S* = 3/2 states, and 130 of the *S* = 1/2 states were included (RASSI routine).

ACKNOWLEDGMENTS

We acknowledge the DFG-TR 88 "3Met" (project A8) and the Karlsruhe Nano Micro Facility (KNMF, www.kit.edu/knmf) for provision of access to instruments at their laboratories. EMP thanks the Panamanian National System of Investigators (SNI, SENACYT) and the project PFID-FID-2021-60 for support. AN and LC thank CNRS for support.

Competing interests

The authors declare no competing financial interests.

References

(1) Ishikawa, N. Single Molecule Magnet with Single Lanthanide Ion. *Polyhedron* **2007**, *26* (9–11), 2147–2153. https://doi.org/10.1016/j.poly.2006.10.022.
(2) Ishikawa, N.; Sugita, M.; Ishikawa, T.; Koshihara, S.; Kaizu, Y. Lanthanide Double-Decker Complexes Functioning as Magnets at the Single-Molecular Level. *J. Am. Chem. Soc.* **2003**, *125* (29), 8694–8695. https://doi.org/10.1021/ja029629n.
(3) Woodruff, D. N.; Winpenny, R. E. P.; Layfield, R. A. Lanthanide Single-Molecule Magnets. *Chem. Rev.* **2013**, *113* (7), 5110–5148. https://doi.org/10.1021/cr400018q.
(4) Armelao, L.; Quici, S.; Barigelletti, F.; Accorsi, G.; Bottaro, G.; Cavazzini, M.; Tondello, E. Design of Luminescent Lanthanide Complexes: From Molecules to Highly Efficient Photo-Emitting Materials. *Coord. Chem. Rev.* **2010**, *254* (5–6), 487–505. https://doi.org/10.1016/j.ccr.2009.07.025.
(5) Bünzli, J.-C. G.; Piguet, C. Taking Advantage of Luminescent Lanthanide Ions. *Chem. Soc. Rev.* **2005**, *34* (12), 1048. https://doi.org/10.1039/b406082m.
(6) Guo, F.-S.; Day, B. M.; Chen, Y.-C.; Tong, M.-L.; Mansikkamäki, A.; Layfield, R. A. Magnetic Hysteresis up to 80 Kelvin in a Dysprosium Metallocene Single-Molecule Magnet. *Science* **2018**, *362* (6421), 1400–1403. https://doi.org/10.1126/science.aav0652.
(7) Gould, C. A.; McClain, K. R.; Reta, D.; Kragskow, J. G. C.; Marchiori, D. A.; Lachman, E.; Choi, E.-S.; Analytis, J. G.; Britt, R. D.; Chilton, N. F.; Harvey, B. G.; Long, J. R. Ultrahard Magnetism from Mixed-Valence Dilanthanide Complexes with Metal-Metal Bonding. *Science* **2022**, *375* (6577), 198–202. https://doi.org/10.1126/science.abl5470.

(8) Goodwin, C. A. P.; Ortu, F.; Reta, D.; Chilton, N. F.; Mills, D. P. Molecular Magnetic Hysteresis at 60 Kelvin in Dysprosocenium. *Nature* **2017**, *548* (7668), 439–442. https://doi.org/10.1038/nature23447.
(9) Moreno-Pineda, E.; Godfrin, C.; Balestro, F.; Wernsdorfer, W.; Ruben, M. Molecular Spin Qudits for Quantum Algorithms. *Chem. Soc. Rev.* **2018**, *47* (2), 501–513. https://doi.org/10.1039/C5CS00933B.
(10) Moreno-Pineda, E.; Klyatskaya, S.; Du, P.; Damjanović, M.; Taran, G.; Wernsdorfer, W.; Ruben, M. Observation of Cooperative Electronic Quantum Tunneling: Increasing Accessible Nuclear States in a Molecular Qudit. *Inorg. Chem.* **2018**, *57* (16), 9873–9879. https://doi.org/10.1021/acs.inorgchem.8b00823.
(11) Gaita-Ariño, A.; Luis, F.; Hill, S.; Coronado, E. Molecular Spins for Quantum Computation. *Nat. Chem.* **2019**, *11* (4), 301–309. https://doi.org/10.1038/s41557-019-0232-y.
(12) Moreno-Pineda, E.; Wernsdorfer, W. Measuring Molecular Magnets for Quantum Technologies. *Nat. Rev. Phys.* **2021**, *3* (9), 645–659. https://doi.org/10.1038/s42254-021-00340-3.
(13) Bogani, L.; Wernsdorfer, W. Molecular Spintronics Using Single-Molecule Magnets. *Nat. Mater.* **2008**, *7* (3), 179–186. https://doi.org/10.1038/nmat2133.
(14) Urdampilleta, M.; Klyatskaya, S.; Cleuziou, J.-P.; Ruben, M.; Wernsdorfer, W. Supramolecular Spin Valves. *Nat. Mater.* **2011**, *10* (7), 502–506. https://doi.org/10.1038/nmat3050.
(15) Wagner, S.; Kisslinger, F.; Ballmann, S.; Schramm, F.; Chandrasekar, R.; Bodenstein, T.; Fuhr, O.; Secker, D.; Fink, K.; Ruben, M.; Weber, H. B. Switching of a Coupled Spin Pair in a Single-Molecule Junction. *Nat. Nanotechnol.* **2013**, *8* (8), 575–579. https://doi.org/10.1038/nnano.2013.133.
(16) Thiele, S.; Balestro, F.; Ballou, R.; Klyatskaya, S.; Ruben, M.; Wernsdorfer, W. Electrically Driven Nuclear Spin Resonance in Single-Molecule Magnets. *Science* **2014**, *344* (6188), 1135–1138. https://doi.org/10.1126/science.1249802.
(17) Vincent, R.; Klyatskaya, S.; Ruben, M.; Wernsdorfer, W.; Balestro, F. Electronic Read-out of a Single Nuclear Spin Using a Molecular Spin Transistor. *Nature* **2012**, *488* (7411), 357–360. https://doi.org/10.1038/nature11341.
(18) Feng, M.; Tong, M.-L. Single Ion Magnets from 3d to 5f: Developments and Strategies. *Chem. - Eur. J.* **2018**, *24* (30), 7574–7594. https://doi.org/10.1002/chem.201705761.
(19) Zhang, P.; Guo, Y.-N.; Tang, J. Recent Advances in Dysprosium-Based Single Molecule Magnets: Structural Overview and Synthetic Strategies. *Coord. Chem. Rev.* **2013**, *257* (11–12), 1728–1763. https://doi.org/10.1016/j.ccr.2013.01.012.
(20) Gupta, S. K.; Murugavel, R. Enriching Lanthanide Single-Ion Magnetism through Symmetry and Axiality. *Chem. Commun.* **2018**, *54* (30), 3685–3696. https://doi.org/10.1039/C7CC09956H.
(21) Ungur, L.; Chibotaru, L. F. Strategies toward High-Temperature Lanthanide-Based Single-Molecule Magnets. *Inorg. Chem.* **2016**, *55* (20), 10043–10056. https://doi.org/10.1021/acs.inorgchem.6b01353.
(22) Sessoli, R.; Powell, A. K. Strategies towards Single Molecule Magnets Based on Lanthanide Ions. *Coord. Chem. Rev.* **2009**, *253* (19–20), 2328–2341. https://doi.org/10.1016/j.ccr.2008.12.014.
(23) Scherthan, L.; Schmidt, S. F. M.; Auerbach, H.; Hochdörffer, T.; Wolny, J. A.; Bi, W.; Zhao, J.; Hu, M. Y.; Toellner, T.; Alp, E. E.; Brown, D. E.; Anson, C. E.; Powell, A. K.; Schünemann, V. ^{161}Dy Time- Domain Synchrotron Mössbauer Spectroscopy for Investigating Single- Molecule Magnets Incorporating Dy Ions. *Angew. Chem. Int. Ed.* **2019**, *58* (11), 3444–3449. https://doi.org/10.1002/anie.201810505.

(24) Bünzli, J.-C. G. On the Design of Highly Luminescent Lanthanide Complexes. *Coord. Chem. Rev.* **2015**, *293–294*, 19–47. https://doi.org/10.1016/j.ccr.2014.10.013.
(25) Sy, M.; Nonat, A.; Hildebrandt, N.; Charbonnière, L. J. Lanthanide-Based Luminescence Biolabelling. *Chem. Commun.* **2016**, *52* (29), 5080–5095. https://doi.org/10.1039/C6CC00922K.
(26) Tangoulis, V.; Nastopoulos, V.; Panagiotou, N.; Tasiopoulos, A.; Itskos, G.; Athanasiou, M.; Moreno-Pineda, E.; Wernsdorfer, W.; Schulze, M.; Malina, O. High-Performance Luminescence Thermometer with Field-Induced Slow Magnetic Relaxation Based on a Heterometallic Cyanido-Bridged 3d–4f Complex. *Inorg. Chem.* **2022**, *61* (5), 2546–2557. https://doi.org/10.1021/acs.inorgchem.1c03432.
(27) Karachousos-Spiliotakopoulos, K.; Tangoulis, V.; Panagiotou, N.; Tasiopoulos, A.; Moreno-Pineda, E.; Wernsdorfer, W.; Schulze, M.; Botas, A. M. P.; Carlos, L. D. Luminescence Thermometry and Field Induced Slow Magnetic Relaxation Based on a near Infrared Emissive Heterometallic Complex. *Dalton Trans.* **2022**, *51* (21), 8208–8216. https://doi.org/10.1039/D2DT00936F.
(28) Ding, Y.-S.; Deng, Y.-F.; Zheng, Y.-Z. The Rise of Single-Ion Magnets as Spin Qubits. *Magnetochemistry* **2016**, *2* (4), 40. https://doi.org/10.3390/magnetochemistry2040040.
(29) Pedersen, K. S.; Ariciu, A.-M.; McAdams, S.; Weihe, H.; Bendix, J.; Tuna, F.; Piligkos, S. Toward Molecular 4f Single-Ion Magnet Qubits. *J. Am. Chem. Soc.* **2016**, *138* (18), 5801–5804. https://doi.org/10.1021/jacs.6b02702.
(30) Escalera-Moreno, L.; Baldoví, J. J.; Gaita-Ariño, A.; Coronado, E. Spin States, Vibrations and Spin Relaxation in Molecular Nanomagnets and Spin Qubits: A Critical Perspective. *Chem. Sci.* **2018**, *9* (13), 3265–3275. https://doi.org/10.1039/C7SC05464E.
(31) Wernsdorfer, W.; Ruben, M. Synthetic Hilbert Space Engineering of Molecular Qu *d* Its: Isotopologue Chemistry. *Adv. Mater.* **2019**, *31* (26), 1806687. https://doi.org/10.1002/adma.201806687.
(32) Jenkins, M. D.; Duan, Y.; Diosdado, B.; García-Ripoll, J. J.; Gaita-Ariño, A.; Giménez-Saiz, C.; Alonso, P. J.; Coronado, E.; Luis, F. Coherent Manipulation of Three-Qubit States in a Molecular Single-Ion Magnet. *Phys. Rev. B* **2017**, *95* (6), 064423. https://doi.org/10.1103/PhysRevB.95.064423.
(33) Ferrando-Soria, J.; Moreno Pineda, E.; Chiesa, A.; Fernandez, A.; Magee, S. A.; Carretta, S.; Santini, P.; Vitorica-Yrezabal, I. J.; Tuna, F.; Timco, G. A.; McInnes, E. J. L.; Winpenny, R. E. P. A Modular Design of Molecular Qubits to Implement Universal Quantum Gates. *Nat. Commun.* **2016**, *7* (1), 11377. https://doi.org/10.1038/ncomms11377.
(34) Biard, H.; Moreno-Pineda, E.; Ruben, M.; Bonet, E.; Wernsdorfer, W.; Balestro, F. Increasing the Hilbert Space Dimension Using a Single Coupled Molecular Spin. *Nat. Commun.* **2021**, *12* (1), 4443. https://doi.org/10.1038/s41467-021-24693-6.
(35) Moreno- Pineda, E.; Damjanović, M.; Fuhr, O.; Wernsdorfer, W.; Ruben, M. Nuclear Spin Isomers: Engineering a $Et_4N[DyPc_2]$ Spin Qudit. *Angew. Chem. Int. Ed.* **2017**, *56* (33), 9915–9919. https://doi.org/10.1002/anie.201706181.
(36) Moreno-Pineda, E.; Taran, G.; Wernsdorfer, W.; Ruben, M. Quantum Tunnelling of the Magnetisation in Single-Molecule Magnet Isotopologue Dimers. *Chem. Sci.* **2019**, *10* (19), 5138–5145. https://doi.org/10.1039/C9SC01062A.
(37) Godfrin, C.; Ferhat, A.; Ballou, R.; Klyatskaya, S.; Ruben, M.; Wernsdorfer, W.; Balestro, F. Operating Quantum States in Single Magnetic Molecules: Implementation of Grover's Quantum Algorithm. *Phys. Rev. Lett.* **2017**, *119* (18), 187702. https://doi.org/10.1103/PhysRevLett.119.187702.
(38) Binnemans, K. Interpretation of Europium(III) Spectra. *Coord. Chem. Rev.* **2015**, *295*, 1–45. https://doi.org/10.1016/j.ccr.2015.02.015.

(39) Utochnikova, V. V.; Kalyakina, A. S.; Bushmarinov, I. S.; Vashchenko, A. A.; Marciniak, L.; Kaczmarek, A. M.; Van Deun, R.; Bräse, S.; Kuzmina, N. P. Lanthanide 9-Anthracenate: Solution Processable Emitters for Efficient Purely NIR Emitting Host-Free OLEDs. *J. Mater. Chem. C* **2016**, *4* (41), 9848–9855. https://doi.org/10.1039/C6TC03586H.
(40) He, H. Near-Infrared Emitting Lanthanide Complexes of Porphyrin and BODIPY Dyes. *Coord. Chem. Rev.* **2014**, *273–274*, 87–99. https://doi.org/10.1016/j.ccr.2013.11.006.
(41) Hu, J.-Y.; Ning, Y.; Meng, Y.-S.; Zhang, J.; Wu, Z.-Y.; Gao, S.; Zhang, J.-L. Highly Near-IR Emissive Ytterbium(III) Complexes with Unprecedented Quantum Yields. *Chem. Sci.* **2017**, *8* (4), 2702–2709. https://doi.org/10.1039/C6SC05021B.
(42) George, T. M.; Varughese, S.; Reddy, M. L. P. Near-Infrared Luminescence of Nd^{3+} and Yb^{3+} Complexes Using a Polyfluorinated Pyrene-Based β-Diketonate Ligand. *RSC Adv.* **2016**, *6* (73), 69509–69520. https://doi.org/10.1039/C6RA12220E.
(43) Feng, J.; Zhang, H. Hybrid Materials Based on Lanthanide Organic Complexes: A Review. *Chem Soc Rev* **2013**, *42* (1), 387–410. https://doi.org/10.1039/C2CS35069F.
(44) Fataftah, M. S.; Bayliss, S. L.; Laorenza, D. W.; Wang, X.; Phelan, B. T.; Wilson, C. B.; Mintun, P. J.; Kovos, B. D.; Wasielewski, M. R.; Han, S.; Sherwin, M. S.; Awschalom, D. D.; Freedman, D. E. Trigonal Bipyramidal V^{3+} Complex as an Optically Addressable Molecular Qubit Candidate. *J. Am. Chem. Soc.* **2020**, *142* (48), 20400–20408. https://doi.org/10.1021/jacs.0c08986.
(45) Atzori, M.; Santanni, F.; Breslavetz, I.; Paillot, K.; Caneschi, A.; Rikken, G. L. J. A.; Sessoli, R.; Train, C. Magnetic Anisotropy Drives Magnetochiral Dichroism in a Chiral Molecular Helix Probed with Visible Light. *J. Am. Chem. Soc.* **2020**, *142* (32), 13908–13916. https://doi.org/10.1021/jacs.0c06166.
(46) Bayliss, S. L.; Laorenza, D. W.; Mintun, P. J.; Kovos, B. D.; Freedman, D. E.; Awschalom, D. D. Optically Addressable Molecular Spins for Quantum Information Processing. *Science* **2020**, *370* (6522), 1309–1312. https://doi.org/10.1126/science.abb9352.
(47) Wojnar, M. K.; Laorenza, D. W.; Schaller, R. D.; Freedman, D. E. Nickel(II) Metal Complexes as Optically Addressable Qubit Candidates. *J. Am. Chem. Soc.* **2020**, *142* (35), 14826–14830. https://doi.org/10.1021/jacs.0c06909.
(48) Kumar, K. S.; Serrano, D.; Nonat, A. M.; Heinrich, B.; Karmazin, L.; Charbonnière, L. J.; Goldner, P.; Ruben, M. Optical Spin-State Polarization in a Binuclear Europium Complex towards Molecule-Based Coherent Light-Spin Interfaces. *Nat. Commun.* **2021**, *12* (1), 2152. https://doi.org/10.1038/s41467-021-22383-x.
(49) Serrano, D.; Kuppusamy, S. K.; Heinrich, B.; Fuhr, O.; Hunger, D.; Ruben, M.; Goldner, P. Ultra-Narrow Optical Linewidths in Rare-Earth Molecular Crystals. *Nature* **2022**, *603* (7900), 241–246. https://doi.org/10.1038/s41586-021-04316-2.
(50) Nonat, A.; Bahamyirou, S.; Lecointre, A.; Przybilla, F.; Mély, Y.; Platas-Iglesias, C.; Camerel, F.; Jeannin, O.; Charbonnière, L. J. Molecular Upconversion in Water in Heteropolynuclear Supramolecular Tb/Yb Assemblies. *J. Am. Chem. Soc.* **2019**, *141* (4), 1568–1576. https://doi.org/10.1021/jacs.8b10932.
(51) Nonat, A.; Chan, C. F.; Liu, T.; Platas-Iglesias, C.; Liu, Z.; Wong, W.-T.; Wong, W.-K.; Wong, K.-L.; Charbonnière, L. J. Room Temperature Molecular up Conversion in Solution. *Nat. Commun.* **2016**, *7* (1), 11978. https://doi.org/10.1038/ncomms11978.
(52) Long, J.; Guari, Y.; Ferreira, R. A. S.; Carlos, L. D.; Larionova, J. Recent Advances in Luminescent Lanthanide Based Single-Molecule Magnets. *Coord. Chem. Rev.* **2018**, *363*, 57–70. https://doi.org/10.1016/j.ccr.2018.02.019.

(53) Marin, R.; Brunet, G.; Murugesu, M. Shining New Light on Multifunctional Lanthanide Single- Molecule Magnets. *Angew. Chem. Int. Ed.* **2021**, *60* (4), 1728–1746. https://doi.org/10.1002/anie.201910299.
(54) Jia, J.-H.; Li, Q.-W.; Chen, Y.-C.; Liu, J.-L.; Tong, M.-L. Luminescent Single-Molecule Magnets Based on Lanthanides: Design Strategies, Recent Advances and Magneto-Luminescent Studies. *Coord. Chem. Rev.* **2019**, *378*, 365–381. https://doi.org/10.1016/j.ccr.2017.11.012.
(55) Gálico, D. A.; Marin, R.; Brunet, G.; Errulat, D.; Hemmer, E.; Sigoli, F. A.; Moilanen, J. O.; Murugesu, M. Triplet- State Position and Crystal- Field Tuning in Opto- Magnetic Lanthanide Complexes: Two Sides of the Same Coin. *Chem. – Eur. J.* **2019**, *25* (64), 14625–14637. https://doi.org/10.1002/chem.201902837.
(56) Mamontova, E.; Long, J.; Ferreira, R.; Botas, A.; Luneau, D.; Guari, Y.; Carlos, L.; Larionova, J. Magneto-Luminescence Correlation in the Textbook Dysprosium(III) Nitrate Single-Ion Magnet. *Magnetochemistry* **2016**, *2* (4), 41. https://doi.org/10.3390/magnetochemistry2040041.
(57) Norel, L.; Darago, L. E.; Le Guennic, B.; Chakarawet, K.; Gonzalez, M. I.; Olshansky, J. H.; Rigaut, S.; Long, J. R. A Terminal Fluoride Ligand Generates Axial Magnetic Anisotropy in Dysprosium Complexes. *Angew. Chem. Int. Ed.* **2018**, *57* (7), 1933–1938. https://doi.org/10.1002/anie.201712139.
(58) Vijayakumar, M.; Marimuthu, K.; Sudarsan, V. Concentration Dependent Spectroscopic Behavior of Sm3+ Doped Leadfluoro-Borophosphate Glasses for Laser and LED Applications. *J. Alloys Compd.* **2015**, *647*, 209–220. https://doi.org/10.1016/j.jallcom.2015.06.064.
(59) Chilton, N. F.; Anderson, R. P.; Turner, L. D.; Soncini, A.; Murray, K. S. PHI: A Powerful New Program for the Analysis of Anisotropic Monomeric and Exchange-Coupled Polynuclear *d* - and *f* -Block Complexes. *J. Comput. Chem.* **2013**, *34* (13), 1164–1175. https://doi.org/10.1002/jcc.23234.
(60) Aquilante, F.; Autschbach, J.; Carlson, R. K.; Chibotaru, L. F.; Delcey, M. G.; De Vico, L.; Fdez. Galván, I.; Ferré, N.; Frutos, L. M.; Gagliardi, L.; Garavelli, M.; Giussani, A.; Hoyer, C. E.; Li Manni, G.; Lischka, H.; Ma, D.; Malmqvist, P. Å.; Müller, T.; Nenov, A.; Olivucci, M.; Pedersen, T. B.; Peng, D.; Plasser, F.; Pritchard, B.; Reiher, M.; Rivalta, I.; Schapiro, I.; Segarra- Martí, J.; Stenrup, M.; Truhlar, D. G.; Ungur, L.; Valentini, A.; Vancoillie, S.; Veryazov, V.; Vysotskiy, V. P.; Weingart, O.; Zapata, F.; Lindh, R. MOLCAS 8: New Capabilities for Multiconfigurational Quantum Chemical Calculations across the Periodic Table. *J. Comput. Chem.* **2016**, *37* (5), 506–541. https://doi.org/10.1002/jcc.24221.
(61) Siegbahn, P. E. M.; Almlöf, J.; Heiberg, A.; Roos, B. O. The Complete Active Space SCF (CASSCF) Method in a Newton–Raphson Formulation with Application to the HNO Molecule. *J. Chem. Phys.* **1981**, *74* (4), 2384–2396. https://doi.org/10.1063/1.441359.
(62) Olsen, J.; Roos, B. O.; Jo/rgensen, P.; Jensen, H. J. Aa. Determinant Based Configuration Interaction Algorithms for Complete and Restricted Configuration Interaction Spaces. *J. Chem. Phys.* **1988**, *89* (4), 2185–2192. https://doi.org/10.1063/1.455063.
(63) Lunghi, A.; Totti, F.; Sanvito, S.; Sessoli, R. Intra-Molecular Origin of the Spin-Phonon Coupling in Slow-Relaxing Molecular Magnets. *Chem. Sci.* **2017**, *8* (9), 6051–6059. https://doi.org/10.1039/C7SC02832F.
(64) Sheldrick, G. M. *SHELXT* – Integrated Space-Group and Crystal-Structure Determination. *Acta Crystallogr. Sect. Found. Adv.* **2015**, *71* (1), 3–8. https://doi.org/10.1107/S2053273314026370.

(65) Sheldrick, G. M. Crystal Structure Refinement with *SHELXL*. *Acta Crystallogr. Sect. C Struct. Chem.* **2015**, *71* (1), 3–8. https://doi.org/10.1107/S2053229614024218.
(66) Wang, Z.; Liu, N.; Li, H.; Chen, P.; Yan, P. The Role of Blue- Emissive 1,8- Naphthalimidopyridine *N*- Oxide in Sensitizing Eu^{III} Photoluminescence in Dimeric Hexafluoroacetylacetonate Complexes. *Eur. J. Inorg. Chem.* **2017**, *2017* (15), 2211–2219. https://doi.org/10.1002/ejic.201700019.